OPEN ACCESS
IOP Publishing
Journal of Physics: Condensed Matter
J. Phys.: Condens. Matter **36** (2024) 075801 (11pp)
https://doi.org/10.1088/1361-648X/ad0a13

Tuning of the magneto-caloric effects in $Ni_{43}Mn_{46}In_{11}$ magnetic shape memory alloys by substitution of boron

Senem Saritaş[1], Mert Miraç Çiçek[1,2], Eyup Kavak[1], Kubra Gurpinar[3], Oğuz Yildirim[4], Suheyla Yuce[5], Orhan Atakol[3] and Baris Emre[1,*]

[1] Faculty of Engineering, Department of Engineering Physics, Ankara University, 06100 Beşevler, Ankara, Turkey
[2] REHIS LTCC and Thin Film Department, Aselsan Inc., Ankara 06830, Turkey
[3] Department of Chemistry, Faculty of Science, Ankara University, Ankara 06100, Turkey
[4] Empa-Swiss Federal Laboratories for Material Science and Technology, CH, 8600 Dübendorf, Switzerland
[5] Department of Physics, Science and Literature Faculty, Ondokuz Mayis University, Kurupelit, 55139 Samsun, Turkey

E-mail: bemre@eng.ankara.edu.tr

Received 2 June 2023, revised 31 October 2023
Accepted for publication 6 November 2023
Published 15 November 2023

Abstract

In this study, we report the structural, magnetic, and magnetocaloric properties of B substitution on the Mn site in $Ni_{43}Mn_{46-x}B_xIn_{11}$($x = 0.5$, 1.0) Heusler alloys. Crystal structure analysis using room-temperature x-ray diffraction data reveals both samples have mixed phases composed of cubic and tetragonal phases. The structural and magnetic phase transition characteristic temperatures are determined using differential scanning calorimetry, isothermal magnetization (MT), and isofield magnetization (MH) measurements. Both alloys exhibit inverse and direct magnetocaloric effects in the vicinity of their magnetostructural transition and Curie temperature (T_C), respectively. For $Ni_{43}Mn_{45.0}B_{1.0}In_{11}$ a maximum magnetic entropy change of 25.06 J kg^{-1} K^{-1} is observed at 250 K for a magnetic field change of 5 T.

Keywords: magnetic shape memory alloys, martensitic transformation, magnetocaloric effect, inverse magnetocaloric effect, Heusler alloys

1. Introduction

Magnetic shape memory alloys (MSMAs) are a class of smart materials that exhibit a unique combination of magnetic, shape memory, and mechanical properties. These alloys can undergo large strains when subjected to magnetic fields, making them suitable for various applications, including actuators, sensors, and energy-harvesting devices. The strong magneto-structural, thermo-mechanical, and magneto-thermal coupling of NiMnX (X=In, Ga, Sn, Sb, Al) MSMAs have been shown to exhibit a wide range of unique features over the past ten years. The investigated phenomena comprise magnetization reversal through magnetic field-induced martensite reorientation [1–4], thermal energy generation and absorption via reversible phase transformation latent heat [5, 6], magnetic field-induced martensitic transformation leading to large reversible macroscopic shape change [3, 7, 8], magnetic exchange bias effects [9, 10], as well as giant magnetoresistance [11]. One particularly exciting application of MSMAs is magnetocaloric cooling, which involves manipulating a material's temperature using a magnetic field. This phenomenon is based on the

* Author to whom any correspondence should be addressed.

magnetic entropy change (ΔS_M) that occurs upon applying or removing a magnetic field. MSMAs exhibit large ΔS_M values, which makes them promising candidates for magnetocaloric cooling applications. Owing to its environmental friendliness and superior efficiency, magnetic refrigeration based on the magnetocaloric effect (MCE) of specific substances is a promising substitute for the conventional cooling technology based on vapor compression, which generates ozone-depleting or greenhouse gases and in the literature, there exist several studies reviewing the MCE [5, 12–20]. The development of high-performance magnetocaloric materials is critical for pushing forward the magnetic refrigeration technology that has been receiving a great deal of attention lately.

MSMAs undergoing a structural (martensitic) transition which involves a change in both structural and magnetic properties of the solid. Associated with this first-order magnetostructural transition, these materials display large MCE [21]. Among the MSMAs, Ni-Mn-X based Heusler alloys are MSMAs and exhibit interesting magnetic and magnetocaloric properties and these properties of Ni-Mn-X based Heusler alloys strongly depend on their chemical composition and crystal structure. Typically, these alloys exhibit a ferromagnetic order and show a high degree of spin polarization, which makes them ideal candidates for various magnetic applications, such as spintronics, magnetic recording, and magnetic refrigeration [3, 13, 16, 22]. Due to the large magnetization difference between the martensite and austenite phases in these alloys, the magnetic energy during the phase transition causes a great contribution to the change of the Gibbs free energy, thus causing the magnetic field forced phase transition to be observed. Consequently, during phase transition, the magnetic field is driven by the enormous thermodynamic propulsive force that is generated by the significant magnetization difference between the two phases in these alloys [3]. These materials' physical properties are significantly affected by their chemical composition, enabling the coupling of the second-order magnetic transition with the first-order structural change, thereby amplifying the MCE [23]. In addition, the competition of structural and magnetic entropy change contributions was reported in recent studies where lattice entropy is dominating and magnetic entropy is non-synergetic with it, ultimately revealing the dilemma of inverse magnetocaloric materials [24, 25].

The full Heusler $Ni_{50}Mn_{25}In_{25}$ has a cubic structure and undergoes a martensitic transformation upon cooling below its transformation temperature and the alloys with In content in the range $15 \leqslant x \leqslant 16$ show magnetic-field induced structural transition [26]. Previous studies have reported in Ni-Mn-In and Ni-Mn-Sn changing composition from full Heusler type (X_2YZ) to off-stoichiometric alloys with excess Mn content affect the magnetization difference. It has been shown that initial Mn atoms appear in the Y sublatticeΔ meanwhile excess Mn atoms prefer to be located in the Z sublattice, thereby one can observe strong Mn-Mn antiferromagnetic interactions. Ni-Mn hybridization bond distance plays an important role in addressing the magnetic interaction strength. Several studies reported the large MCE when the ferromagnetic austenite transforms into a weak magnetic (antiferromagnetic/ferrimagnetic) martensite, undergoing first-order magnetostructural transformation, a significant latent heat can be obtained, which is beneficial for achieving large magnetic entropy change (ΔS_m) or adiabatic temperature change (ΔT_{ad}) upon the application of a magnetic field [27–32]. One of the most common ways of changing ferromagnetic interactions is non-magnetic transition metal substitution instead of Mn which leads to change in ferromagnetic interactions that adversely affect the total entropy change [33–36]. Furthermore, it was stated that $Ni_{43}Mn_{46}In_{11}$ undergoes structural transition with temperatures of Ms = 318 K, M_f = 291 K, A_s = 308 K, A_f = 324 K, and the Curie temperature of the austenite phase was observed at 325 K [36]. It was reported in several studies that, substituting of Mn with non-magnetic transition metal affects the lattice size, e/a ratios, which in turn influenced the Mn–Mn exchange interactions, magnetic properties, and martensitic transitions [33, 34, 36–39]. Eventually, increasing B-content decreases both the martensitic transition temperatures and the Curie temperature [34, 37–39]. In this paper, we reported the effect of partially substituting of Mn by B on the structural, thermal, phase transformation, magnetic behaviors, and magnetocaloric properties in $Ni_{43}Mn_{46-x}B_xIn_{11}$ (x = 0.5,1.0) MSMAs.

2. Experimental details

High purity nickel (99.99%), boron (99.90%), manganese (99.99%), and indium (99.99%) elements were used to prepare $Ni_{43}Mn_{46-x}B_xIn_{11}$ (x = 0.5, 1.0) polycrystalline alloys. Conventional arc melting technique used in an argon atmosphere in a water-cooled Cu crucible. To ensure better homogeneity of the samples, ingots were inverted and melted again and the processes were repeated four times. The weight loss in the samples was found to be less than %3 of the initial weight. The ingots were annealed in (evacuated) quartz tubes with argon at 1073 K for 120 h and then quenched into ice water. Microstructures of the samples were studied with the scanning electron microscopy (SEM) technique using both secondary electrons (SEs) and back-scattered electrons (BSEs) signals. The compositions of the $Ni_{43}Mn_{46-x}B_xIn_{11}$ (x = 0.5, 1.0) alloys were determined by energy dispersive x-ray spectroscopy by using the ZEISS EVO 40 system. X-ray diffraction (XRD) experiments were performed using a Rigaku D-Max 2200 with Mo-Kα radiation at room temperature, determining the crystal structures of the alloys. The data obtained were analyzed using the profile-matching program *FullProf* based on the Rietveld method. The thermal martensite and magnetic transitions of the samples were identified (characterized) by differential scanning calorimetry (DSC) where a rate of 10 K min^{-1} was used for the cooling and heating cycle. For temperature and magnetic field-dependent magnetization measurements, a physical property measurement system (Quantum Design), equipped with a vibrating sample magnetometer, was employed. The temperature and magnetic field sweep rates were at 2 K min^{-1} and 0.2 mT s^{-1}, respectively. Sample mass was determined with 0.01 mg accuracy before the magnetic measurements and placed into plastic capsules

and measured with a contamination-free half-cylinder brass sample holder. Contamination and the reproducibility of the measurements were regularly controlled as described in [40].

3. Results and discussion

Figure 1 shows SE and BSE images for SEM analysis from $Ni_{43}Mn_{46-x}B_xIn_{11}$ ($x = 0.5, 1.0$) alloys. Table 1 illustrates the average composition calculated from collected data from three different selected areas on the samples. As can be seen from the table 1, the compositions of the $Ni_{43}Mn_{46-x}B_xIn_{11}$ ($x = 0.5, 1.0$) alloys did not differ much from the intended one, except that, for $Ni_{43}Mn_{45.5}B_{0.5}In_{11}$ alloy boron content was detected a little more than the purposed rate. In figure 1 stripes were due to insufficient polishing of the material. Meanwhile, black points refer to minor a third phase. Thereby, the substitution of B resulted in the formation of a third phase, namely, with the B content increasing, the amount of the third phase increased, observed as black spots in figures 1(c) and (d) for $Ni_{43}Mn_{45.3}B_{0.7}In_{11}$ and $Ni_{43}Mn_{45.0}B_{1.0}In_{11}$ alloys, respectively. As the boron ratio increased, the more spots detected.

Figure 2 presents the room temperature powder XRD data and the Rietveld refinement results of the $Ni_{43}Mn_{45.3}B_{0.7}In_{11}$ and $Ni_{43}Mn_{45.0}B_{1.0}In_{11}$ alloys. The lattice parameters, Rp, Rwp, and $\chi 2$ values for the investigated alloys are given in table 2. The crystal structure $Ni_{43}Mn_{46}In_{11}$ alloy showed a single phase with tetragonal (martensite phase) [36], while boron-doped alloys had cubic (austenite phase) and tetragonal (martensite phase) crystal structures. As boron content increased we observed a small increase in the unit cell parameter for tetragonal structure. Meanwhile, for cubic structure we observed an increase in unit cell parameters with increasing boron content. This might be due to the attributed to the increase in the third phase or boron atoms prefer to occupy into the interstitial sites rather than occupation of the Mn sites in the unit cell [41]. At room temperature, the dominant phase in the $Ni_{43}Mn_{45.3}B_{0.7}In_{11}$ and $Ni_{43}Mn_{45.0}B_{1.0}In_{11}$ alloys was found to be tetragonal, while there are still visible traces of the cubic phase near the $(202)_M$ peak. According to the room temperature XRD data, the dominant phase in $Ni_{43}Mn_{45.3}B_{0.7}In_{11}$ and $Ni_{43}Mn_{45.0}B_{1.0}In_{11}$ alloys is found to be tetragonal, while traces of the cubic phase can also be observed, for instance in the $(202)_M$ peak shown in figure 2. In addition, the data given in figure 2, enables us to observe the $(202)_M$ small martensite peak intensity near the $(220)_A$ main cubic phase peak for $Ni_{43}Mn_{45.3}B_{0.7}In_{11}$ and $Ni_{43}Mn_{45.0}B_{1.0}In_{11}$ alloys indicating that martensitic phase transition is close to room temperature. We calculated phase ratio of austenite/martensite according to the peak intensity $\frac{I_{(220)A}}{I_{(202)M}}$. Consequently, we calculated that there existed 93% austenite and 7% martensite for $Ni_{43}Mn_{45.3}B_{0.7}In_{11}$ alloy and 56% austenite and 44% martensite for $Ni_{43}Mn_{45.0}B_{1.0}In_{11}$ alloy. The transition from the parent phase to the martensitic phase typically follows a nucleation and growth process, and the transformation is influenced by various factors such as temperature, stress and material composition. It has also been observed that some NiMn-based alloys, including NiMnIn, especially non-stoichiometric ones, exhibit 'pre-martensitic' or 'incipient martensitic' behavior. This means that some regions within the material may have already undergone martensitic transformation due to factors such as thermal history, local stress or the presence of pre-existing nuclei. These pre-existing martensitic regions can be considered as 'martensitic variants' or 'martensitic embryos' formed during previous thermal cycles or due to local stress conditions. The transformation temperature of these zones may be higher than the overall bulk transformation temperature due to size effects or other factors affecting transformation kinetics [17, 42–45].

Figures 3(a) and (b) shows the DSC curves for the $Ni_{43}Mn_{45.3}B_{0.7}In_{11}$ and $Ni_{43}Mn_{45.0}B_{1.0}In_{11}$ alloys, respectively. The austenite-martensite phase transformations are shown by the exothermic and endothermic peaks, respectively. The results of the tangent method's analysis of the structural phase changes are shown in table 3. The thermal hysteresis, which is calculated using the formula $\Delta T_{hys} = ((A_s + A_f)/2 - (M_s + M_f)/2)$ suggests that phase transformation is first-order. We were not able to monitor the T_C as we had oscillations during the manual pouring of liquid nitrogen.

Figures 4(a) and (b) shows the temperature dependence of magnetization (M(T)) obtained for zero-field cooling (ZFC), field cooling (FC), and field-heating (FH) cycles at applied magnetic fields of 100 Oe of $Ni_{43}Mn_{45.3}B_{0.7}In_{11}$ and $Ni_{43}Mn_{45.0}B_{1.0}In_{11}$ alloys, respectively. For $Ni_{43}Mn_{45.3}B_{0.7}In_{11}$ alloy, while cooling a jump-like increase in magnetization was observed at the Curie temperature ($T_C = 314$ K) from the ferromagnetic austenitic to the paramagnetic austenitic. Upon further decrease the temperature martensitic transition temperature $T_M = 245$ K ($T_M = (A_s + M_f)/2$) concomitantly followed by sharp decrease was observed for magnetization from the ferromagnetic martensite/austenitic to the antiferromagnetic/ferrimagnetic martensitic phase. The same scenario is valid for $Ni_{43}Mn_{45.0}B_{1.0}In_{11}$ alloy, with T_M and T_C of austenite observed, at 253 K and 299 K, respectively. During the cooling, the magnetization increased with decreasing temperature and then decreased abruptly at the martensitic transition $M_s = 267$ K and $M_f = 240$ K, for $Ni_{43}Mn_{45.0}B_{1.0}In_{11}$ alloy. When compare the structural temperatures and Curie temperature of undoped parent alloy and boron doped alloys investigated in this study, it is clear as B ratio increased not only martensite structural transformation temperatures decreased but also Curie temperature decreased towards lower temperatures. Thermal hysteresis is a fingerprint of first-order structural (martensitic) transitions observed in such systems and we calculated thermal hysteresis as 10.0 K and 24.8 K, for $Ni_{43}Mn_{45.3}B_{0.7}In_{11}$ and $Ni_{43}Mn_{45.0}B_{1.0}In_{11}$, respectively. Among the thermal hysteresis the discrepancy between DSC and M(T) data may have resulted from different specimen sizes, slightly different compositions, or different heating and cooling rates. Moreover, the $T_C - T_M$ values of $Ni_{43}Mn_{45.3}B_{0.7}In_{11}$ and $Ni_{43}Mn_{45.0}B_{1.0}In_{11}$ was calculated as 69 K and 46 K, respectively. In addition, prior studies explained the decrease of martensitic temperatures as a consequence of the decrease in the e/a ratio which is valid in

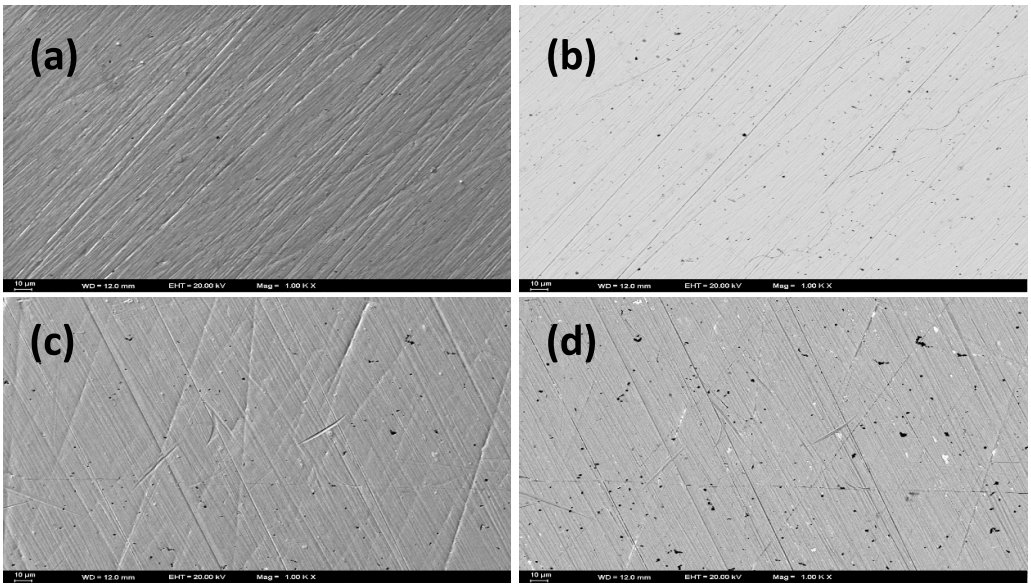

Figure 1. SEM analysis images for (a) and (b) SE and BSE images of $Ni_{43}Mn_{45.3}B_{0.7}In_{11}$ alloy and (c) and (d) SE and BSE images of $Ni_{43}Mn_{45.0}B_{1.0}In_{11}$ alloy.

Table 1. Compositions of $Ni_{43}Mn_{45.3}B_{0.7}In_{11}$ and $Ni_{43}Mn_{45.0}B_{1.0}In_{11}$ alloys determined by EDX analysis.

Alloy	Ni	Mn	B	In	e/a
$Ni_{43}Mn_{45.3}B_{0.7}In_{11}$	42.92 ± 1.1	45.17 ± 1.0	0.69 ± 0.1	11.22 ± 0.6	7.797
$Ni_{43}Mn_{45.0}B_{1.0}In_{11}$	43.01 ± 1.1	44.95 ± 1.0	1.02 ± 0.1	11.02 ± 0.6	7.788

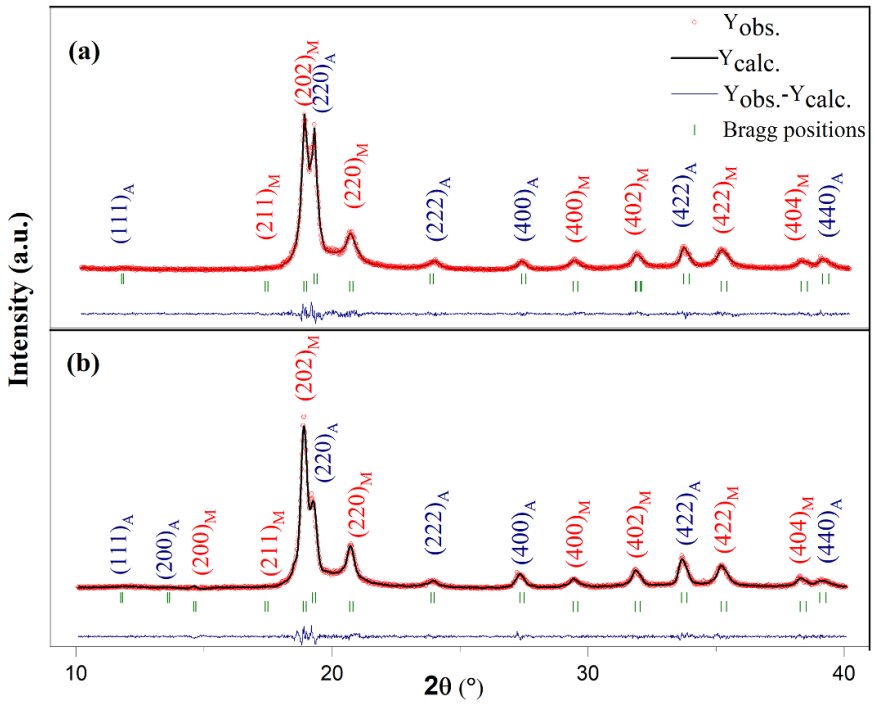

Figure 2. XRD patterns at room temperature for (a) $Ni_{43}Mn_{45.3}B_{0.7}In_{11}$ and (b) $Ni_{43}Mn_{45.0}B_{1.0}In_{11}$ alloys.

this study [26, 46]. Namely, the e/a ratio of the parent alloy, $Ni_{43}Mn_{45.3}B_{0.7}In_{11}$ alloy, and $Ni_{43}Mn_{45.0}B_{1.0}In_{11}$ alloy is calculated as 7.855, 7.797, and 7.788, respectively. In addition, for the Ni–Mn hybridization, any change in the Ni or Mn concentration during fabrication will influence the Ni–Mn distance and hence the hybridization strength. Thus, the martensitic transformation will shift to lower or higher temperatures [37], in this work, B-substitution into the Ni–Mn–In system

Table 2. Unit cell parameters for $Ni_{43}Mn_{45.3}B_{0.7}In_{11}$ and $Ni_{43}Mn_{45.0}B_{1.0}In_{11}$ alloys obtained by Rietveld refinement and comparison to $Ni_{43}Mn_{46}In_{11}$ [28] alloy.

	Crystal structure	a (Å)	b (Å)	c (Å)	V (Å^3)	R_p	R_{wp}	χ^2	References
$Ni_{43}Mn_{46}In_{11}$	Tetragonal (*I4/mmm*)	5.566 (3)	5.566 (3)	6.884 (3)	213.36 (2)	8.5	11.2	1.79	[36]
$Ni_{43}Mn_{45.3}B_{0.7}In_{11}$	Cubic (Fm-3m)	5.987 (2)	5.987 (2)	5.987 (2)	214.67 (2)	6.9	9.6	1.30	This work
$Ni_{43}Mn_{45.0}B_{1.0}In_{11}$	Tetragonal (*I4/mmm*) Cubic (F m -3m) Tetragonal (*I4/mmm*)	5.586 (3) 6.003 (2) 5.586 (3)	5.586 (3) 6.003 (2) 5.586 (3)	6.822 (3) 6.003 (2) 6.841(3)	214.16 (3) 216.30 (2) 213.46(3)	7.1	9.6	1.33	This work

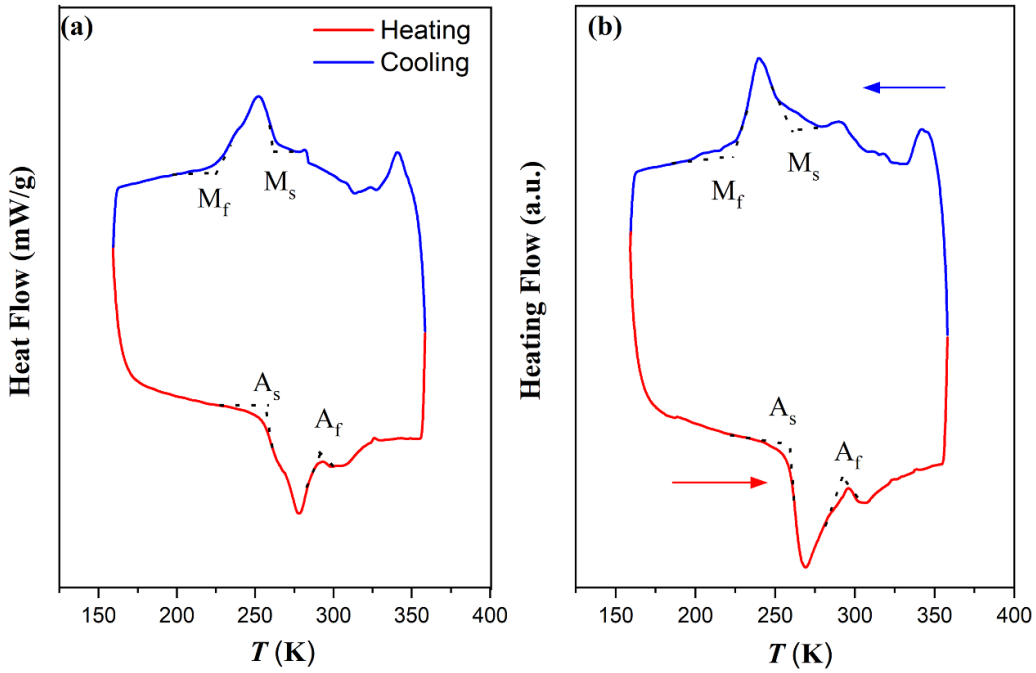

Figure 3. DSC curves for (a) $Ni_{43}Mn_{45.3}B_{0.7}In_{11}$ and (b) $Ni_{43}Mn_{45.0}B_{1.0}In_{11}$alloys.

Table 3. Characteristic austenite and martensite phase transformation temperatures obtained from heating and cooling DSC analysis.

Alloy	A_s (K)	A_f(K)	M_s (K)	M_f (K)	ΔT_{hys} (K)	ΔS_t (J kg^{-1} K^{-1})
$Ni_{43}Mn_{45.3}B_{0.7}In_{11}$	256	295	267	231	32	18.14
$Ni_{43}Mn_{45.0}B_{1.0}In_{11}$	258	294	260	229	33	26.75

indicates the enhanced Ni–Mn hybridization, cause to shift of martensitic transition (T_M) shift to lower temperatures. As table 4 shows, there is a significant difference between the Curie temperature of the parent alloy ($Ni_{43}Mn_{46}In_{11}$), $Ni_{43}Mn_{45.3}B_{0.7}In_{11}$, and $Ni_{43}Mn_{45.0}B_{1.0}In_{11}$ alloys. The reason for this difference might be related to the change in antiferromagnetism between Mn-Mn atoms, and this situation has also been observed in NiMnIn [36], $Ni_{50}Mn_{37-x}Cr_xSb_{13}$ [47] and many NiMnZ (Z=Ga, In, Sn and Sb) systems [48, 49]. The insets of figures 4(a) and (b) shows the low-temperature range M(T) data. Interestingly, at low temperatures, there exists the presence of a peak in the ZFC plot is attributed as a spin glass peak [50, 51], T_G of $Ni_{43}Mn_{45.3}B_{0.7}In_{11}$ and $Ni_{43}Mn_{45.0}B_{1.0}In_{11}$ was observed at 96 K and 91 K, respectively. The existence of spin glass peak was explained to be due to the result of mixed magnetic interactions between ferromagnetic and antiferromagnetic clusters [50, 51]. Among the other things, there exist a hysteresis between FC and FH curves for all applied magnetic fields which is quite evident for 100 Oe measurement reported in our previous studies [25, 52]. Moreover, it is reported that antiferromagnetic exchange leading to local noncollinear spin structures, which can pin the ferromagnetic domains in different configurations [53]. Therefore, we think that this hysteretic behavior is not an actual hysteresis which might be due to complex magnetic behavior or an experimental error. Indeed, it is not possible to determine from the present data what the exact nature of the magnetic coupling is at these temperatures. Further studies using neutron techniques would be required to understand this aspect of the problem.

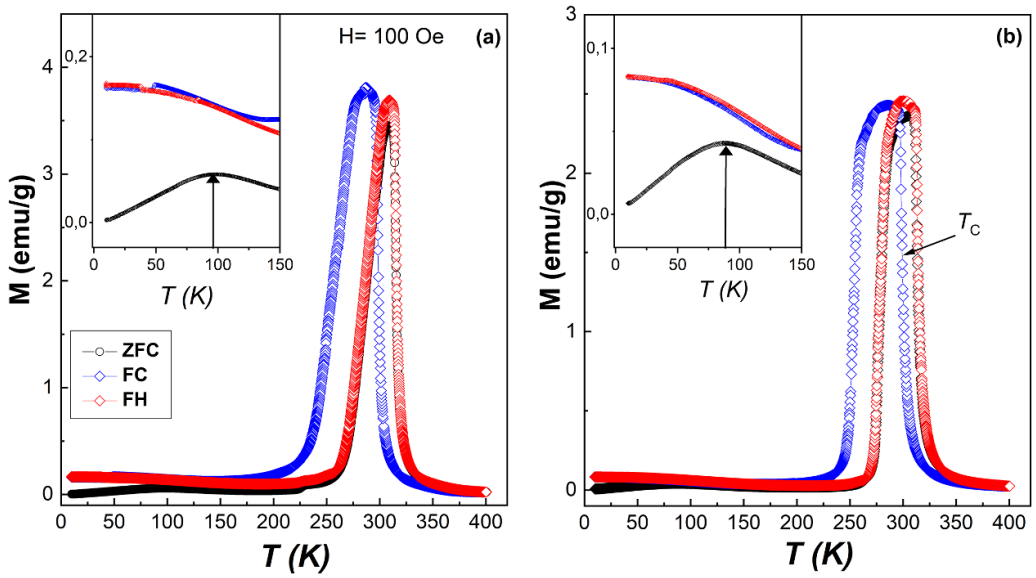

Figure 4. Zero field cooled (ZFC), field cooled (FC), and field heated (FH) mode temperature-dependent magnetization curves in a magnetic field 100 Oe (a) $Ni_{43}Mn_{45.3}B_{0.7}In_{11}$ and (b) $Ni_{43}Mn_{45.0}B_{1.0}In_{11}$ alloys.

Table 4. Thermomagnetic (M(T)) analysis results for $Ni_{43}Mn_{45.3}B_{0.7}In_{11}$ and $Ni_{43}Mn_{45.0}B_{1.0}In_{11}$ alloys.

Alloys	H	M_s (K)	M_f (K)	A_s (K)	A_f (K)	ΔT_{hys} (K)	T_C (K)	T_M (K)	$T_C - T_m$ (K)
$Ni_{43}Mn_{46}In_{11}$	**0.01**	318	291	308	324	10	325	299.5	25.5
$Ni_{43}Mn_{45.3}B_{0.7}In_{11}$	**0.01**	276	230	260	305	10	314	245	69
	0.5	275	229	264	302	33	314	244	70
	1.0	274	228	260	301	33.6	314	244	70
	3.0	272	220	260	300	35	327	240	87
	5.0	267	211	249	298	37.4	327	229	98
	7.0	263	203	243	293	38	327	223	104
$Ni_{43}Mn_{45.0}B_{1.0}In_{11}$	**0.01**	267	240	265	298	24.8	299	253	46
	0.5	260	240	272	290	28.5	311	256	55
	1.0	260	240	270	287	29	314	255	59
	3.0	257	232	262	286	30	314	247	67
	5.0	251	229	259	282	30	327	244	83
	7.0	241	216	245	275	30	338	233	105

Figures 5(a) and (b) shows the thermomagnetization curves M(T) at higher magnetic fields of 0.5 T, 1 T, 3 T, and 5 T of $Ni_{43}Mn_{45.3}B_{0.7}In_{11}$ and $Ni_{43}Mn_{45.0}B_{1.0}In_{11}$ alloys, respectively. From the data in figures 5(a) and (b), it is apparent that with the application of a higher magnetic field, a larger magnetization difference (ΔM) was observed while the martensitic transition. For instance, with the application of 7 T magnetic field, we observed 71 emu g^{-1} and 76 emu g^{-1} ΔM for $Ni_{43}Mn_{45.3}B_{0.7}In_{11}$ and $Ni_{43}Mn_{45.0}B_{1.0}In_{11}$ while heating. Interestingly ΔM during cooling was larger than during heating. XRD refinement studies (table 2) demonstrate that the B-doping of the alloy causes the lattice to contract, leading to a decreased Mn-Mn distance. This is substantiated by the fact that the ΔM in the $Ni_{43}Mn_{45.0}B_{1.0}In_{11}$ alloy is higher than $Ni_{43}Mn_{45.3}B_{0.7}In_{11}$ alloy. The stoichiometric alloy (Ni_2MnIn)'s magnetic behavior is dependent on Mn-Mn, Mn-Ni, and Ni-Ni hybridization, while Mn makes up the majority of the magnetic moment. In Ni_2MnIn alloy, a significantly long Mn-Mn distance promotes indirect interactions such as RKKY or Anderson s-d interactions to mediate ferromagnetism [34, 54]. There are two forms of coupling among Mn atoms in non-stoichiometric alloys with excess Mn residing in In sites: intra-site coupling (between Mn atoms at Mn site) and inter-site coupling (between Mn atoms at Mn and In sites) [54]. The latter is antiferromagnetic, whereas the former is ferromagnetic. The combination of these interactions causes the martensite phase's non-collinear spin structure [55]. Recent research has demonstrated that inter-site contact is stronger in the martensite phase, resulting in its antiferromagnetic ordering, whereas intra-site interaction is stronger in the austenite phase, which is primarily ferromagnetic [56]. Consequently, any variation in the Mn-Mn distance due to the change in the crystallographic configuration can influence the magnitude of the interactions, resulting in different magnetic exchange. Therefore, the bigger ΔM in the $Ni_{43}Mn_{45.0}B_{1.0}In_{11}$ alloy can be credited to the spontaneous

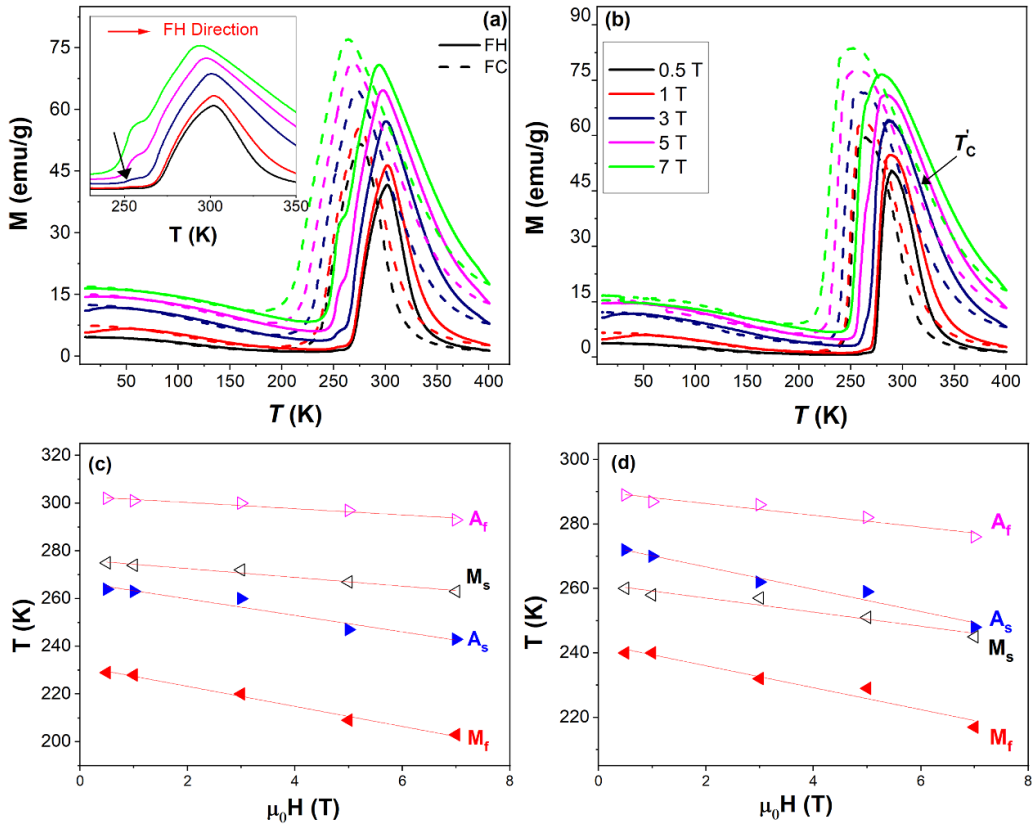

Figure 5. Thermomagnetization (M(T)) curves of (a) $Ni_{43}Mn_{45.3}B_{0.7}In_{11}$ alloy and (b) $Ni_{43}Mn_{45.0}B_{1.0}In_{11}$ alloy under the magnetic fields of 0.5 T, 1 T, 3 T, 5 T, and 7 T. The martensitic transformation temperatures were determined from the M(T) curves (c) $Ni_{43}Mn_{45.3}B_{0.7}In_{11}$ alloy and (d) $Ni_{43}Mn_{45.0}B_{1.0}In_{11}$ alloy. Lines correspond to linear regression to the data.

structural transition better linked with the magnetic transition.

Moreover, from the data in figures 5(a) and (b), with increasing magnetic field, the martensitic transition shifts towards lower temperatures, in agreement with the magnetic field stabilizing the large magnetization cubic (austenite) phase. The characteristic temperature of M_s, M_f, A_s, and A_f linearly decreased with the applied magnetic field at a rate of -1.83 K T^{-1}, -4.20 K T^{-1}, -3.46 K T^{-1}, and -1.31 K T^{-1} for $Ni_{43}Mn_{45.3}B_{0.7}In_{11}$ alloy depicted in figure 5(c). Meanwhile, for $Ni_{43}Mn_{45.0}B_{1.0}In_{11}$ alloy they were calculated as -2.19 K T^{-1}, -3.40 K T^{-1}, -3.46 K T^{-1}, and -1.82 K T^{-1} shown in figure 5(d). In addition, as shown in table 4, the thermal hysteresis increased with the increase of magnetic field. It was shown that the width of the hysteresis changes linearly with martensite-to-austenite proportion [57], therefore, the increase of thermal hysteresis with increase of applied magnetic field might be due to the difficulty of phase front motion between the martensite and austenite strengthened.

It is somewhat surprising that with the applied magnetic field in the temperature interval $T_C > T_M$, we observed a large shift of T_C to the higher temperatures, namely, T_C shifted 28 K and 39 K for $Ni_{43}Mn_{45.3}B_{0.7}In_{11}$ and $Ni_{43}Mn_{45.0}B_{1.0}In_{11}$ alloys, respectively. These results agree with the findings of other studies, in which this behavior was explained by the existence of a non-collinear ferromagnetic structure in the austenitic state [22]. Increasing the external magnetic field will cause a strengthened ferromagnetic component in the austenitic phase and hence an increase in the ferromagnetic component in the austenitic phase, and therefore in the increase of T_C' [22]. Figure 5(a) inset shows that there exists an anomaly around 250 K with the application of 1 T magnetic field. This anomaly shifted to a higher temperature with the application of a higher applied magnetic field. This anomaly was less clearly observed for $Ni_{43}Mn_{45.0}B_{1.0}In_{11}$ alloy in figure 5(b). That anomaly might be related to the mixed magnetic phase as stated by previous studies [22, 50].

Figures 6(a) and (b) illustrates the isothermal magnetization curves M(H) for the magnetization and demagnetization directions of $Ni_{43}Mn_{45.3}B_{0.7}In_{11}$ and $Ni_{43}Mn_{45.0}B_{1.0}In_{11}$, respectively. Figures 6(a) and (b) demonstrates the M(H) curves were carried out with a temperature protocol which is called loop process suggested by Anon Caron *et al* [58] to avoid spurious results induced by the hysteresis of transformation, namely, first samples were initially cooled down to the martensitic transformation temperature in zero magnetic field then the sample heated up to the desired temperatures. In figure 6(a) a metamagnetic transition is observed in the temperature range of 250 K–300 K. The metamagnetic transition manifests the field induced structural transition from the low magnetic martensite phase to the high magnetic austenite phase. In figure 6(b), metamagnetic transition is observed in the temperature range of

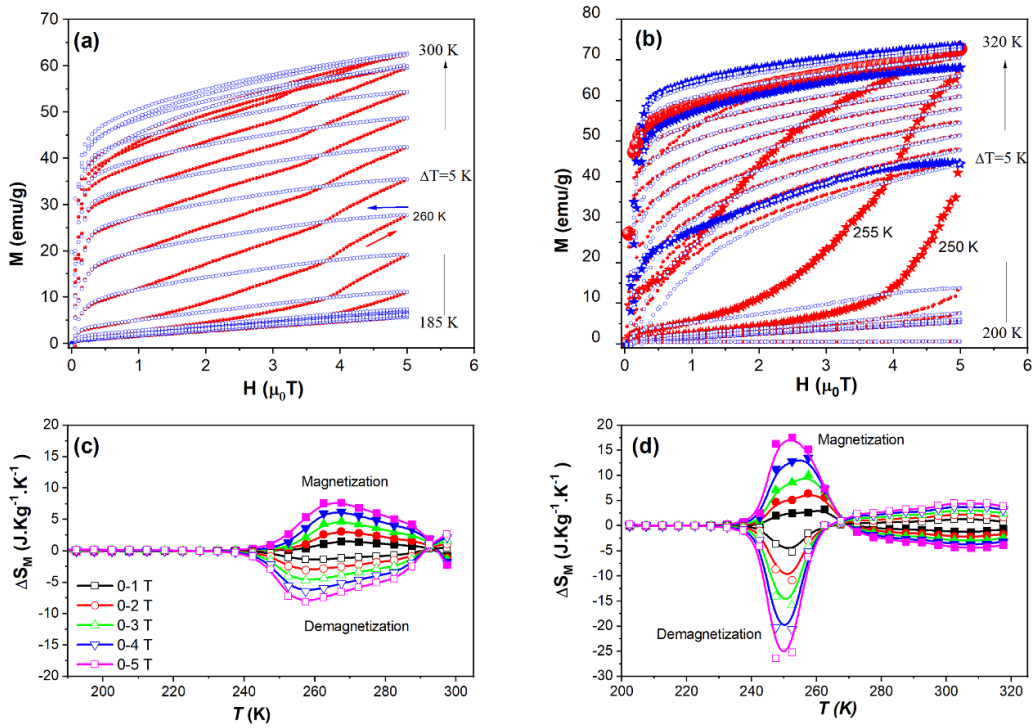

Figure 6. M(H) curves for (a) $Ni_{43}Mn_{45.3}B_{0.7}In_{11}$ and (b) $Ni_{43}Mn_{45.0}B_{1.0}In_{11}$. Magnetic field-induced entropy change (magnetocaloric effect) as a function of temperature for selected values of the magnetic field (1, 2, 3, 4, and 5 T) of (c) $Ni_{43}Mn_{45.3}B_{0.7}In_{11}$ and (d) $Ni_{43}Mn_{45.0}B_{1.0}In_{11}$.

245 K–265 K. The sharpness of the metamagnetic transition in the $Ni_{43}Mn_{45.0}B_{1.0}In_{11}$alloy doped alloy is higher than in the $Ni_{43}Mn_{45.3}B_{0.7}In_{11}$ alloy, which may be due to the sharp martensite transition (figure 5). The critical field to induce the metamagnetic transition for $Ni_{43}Mn_{45.0}B_{1.0}In_{11}$ alloy declined with increasing temperature, the critical field for $Ni_{43}Mn_{45.3}B_{0.7}In_{11}$ alloy was virtually constant (∼3.5 T). Moreover, at practically all metamagnetic transition temperatures, the maximum magnetic hysteresis of 4.0 T was recorded for the $Ni_{43}Mn_{45.3}B_{0.7}In_{11}$ alloy. Meanwhile, for $Ni_{43}Mn_{45.0}B_{1.0}In_{11}$ alloy, the greatest magnetic hysteresis of 4.0 T was noted at 250 K, and it was reduced for other temperatures. Both samples did not saturate even under the magnetic field of 5 T. This might be related to the coexistence of antiferromagnetic exchange within the ferromagnetic matrix due to excess Mn in the crystal structure is the essential source for non-saturation [53].

In addition, the magnetic entropy changes (ΔS_M) as a function of temperature for various applied fields ($\mu_0 \Delta H$) are shown in figures 6(c) and (d). We numerically estimated the magnetic field-induced entropy change (ΔS) around magnetic transition using the relationship $\Delta S_M(T_K, 0 \rightarrow H) = \frac{1}{\Delta T_k}[\int_0^H M_{T_{k+1}} dH - \int_0^H M_{T_k} dH]$ from the M(H) isotherms which is presented in figures 6(a) and (b). The maximum magnetic entropy change values in a magnetic field change of 0–5 T calculated as 7.65 J kg^{-1} K^{-1} and 17.54 J kg^{-1} K^{-1} for magnetization direction and 8.19 J kg^{-1} K^{-1} and 25.06 J kg^{-1} K^{-1} for demagnetization direction $Ni_{43}Mn_{45.3}B_{0.7}In_{11}$ and $Ni_{43}Mn_{45.0}B_{1.0}In_{11}$ alloys, respectively. For both samples, the sign of ΔS_M is positive in the range of MT. In Ni–Mn based Heusler alloys, the magnetic moments are mainly anchored to the Mn atoms and the exchange interaction is strongly dependent on the Mn-Mn distance. Consequently, any alteration in the Mn-Mn distance resulting from a change in the crystallographic configuration can influence the strength of interactions, leading to varying magnetic exchanges [59]. Thus, the higher ΔM in $Ni_{43}Mn_{45.0}B_{1.0}In_{11}$ alloy could be attributed to the spontaneous structural transition coupled with the magnetic transition. The inverse nature of the MCE is consistent with the magnetic field stabilization of the cubic phase and the maximum value of ΔS_M increases with increasing magnetic field. From figures 6(c) and (d) it is clear that close to T_C alloys show negative namely conventional MCE since $\Delta M/\Delta T < 0$ around the second-order magnetic transition.

The calculated values of ΔS_M value of the $Ni_{43}Mn_{45.0}B_{1.0}In_{11}$ alloy is higher than those of $Ni_{43}Mn_{45.3}B_{0.7}In_{11}$, which may be due to: (i) the better coupling of structural and magnetic transitions, (ii) the larger magnetization difference of $Ni_{43}Mn_{45.0}B_{1.0}In_{11}$ alloy, (iii) the sharpness of the field-induced structural phase transition and metamagnetic transition with the applied magnetic field, (iv) and almost complete reversible martensitic transformation under 5 T field loading. To make this last point even clearer, for $Ni_{43}Mn_{45.0}B_{1.0}In_{11}$ alloy, the transition entropy was calculated as 26.75 J kg^{-1} K^{-1} from DSC data, and the magnetic field-induced entropy change for demagnetization was calculated as 25.06 J kg^{-1} K^{-1} which refers that $Ni_{43}Mn_{45.0}B_{1.0}In_{11}$ alloy almost totally transformed while magnetic field induced transition and only a small fraction of the sample remained

as austenite. Meanwhile, for $Ni_{43}Mn_{45.3}B_{0.7}In_{11}$ alloy, the transition entropy was calculated as 18.2 J kg^{-1} K^{-1} from DSC data, and the magnetic field-induced entropy change for demagnetization was calculated as 8.19 J kg^{-1} K^{-1}which shows that during magnetic field induced transition smaller fraction of the $Ni_{43}Mn_{45.3}B_{0.7}In_{11}$ alloy transforms reversibly with respect to $Ni_{43}Mn_{45.0}B_{1.0}In_{11}$ alloy. Therefore, it was reported that by using fractional method on MSMAs the lesser counteract of lattice entropy and magnetic entropy to each other, one can observe higher inverse MCE values which is valid for this study [25]. From the standpoint of the MCE's reversibility, which is connected to the transition's hysteresis and the sensitivity of the transition temperatures to the applied magnetic field (dA_f/dH). A greater degree of reversibility will result from field cycling across a wider temperature range if the martensitic transition temperatures are more sensitive to the applied magnetic field. This situation reveals that the reversibility of MCE increases with the increase in the boron ratio, that is, the reversibility can be improved by tuning the boron ratio. In addition, the values of ΔS_M of $Ni_{43}Mn_{45.0}B_{1.0}In_{11}$ alloy are higher than parent alloy 21.5 kg^{-1} K^{-1} [36] and comparable with other inverse Ni-Mn based alloys at 5 T such as ∼16 J kg^{-1} K^{-1} for $Ni_{50}Mn_{35}In_{13.9}B_{1.1}$ [22], ∼18 J kg^{-1} K^{-1} for $Ni_{50}Mn_{34}B_1In_{15}$ [34], ∼30 J kg^{-1} K^{-1} for $Ni_{47}Mn_{37}Si_3In_{13}$ [33], ∼22.8 J kg^{-1} K^{-1} for $Ni_{46}Co_3Mn_{37}In_{10}Ge_4$ [17], 14.6 J kg^{-1} K^{-1} for $Ni_{49.8}Co_{1.2}Mn_{33.5}In_{15.5}$ [60], 22 J kg^{-1} K^{-1} for $Ni_{43}Mn_{46}Sn_{10.5}B_{0.5}$ [59], 18.9 J kg^{-1} K^{-1} for $Ni_{50}Mn_{35}In_{14.5}B_{0.5}$ [61], 16.0 J kg^{-1} K^{-1} for $Ni_{50}Mn_{35}In_{14.25}B_{0.75}$ [62].

4. Conclusions

To sum up, the magnetic and martensitic transformation behavior of $Ni_{43}Mn_{45.3}B_{0.7}In_{11}$ and $Ni_{43}Mn_{45.0}B_{1.0}In_{11}$ MSMAs were investigated. The addition of a small amount of B led to a sharp decrease in martensitic transformation and T_C temperatures. Thus, the multifunctional properties of these quaternary alloys may be enhanced, tuned, and adjusted by boron addition. Furthermore, the martensite finish temperature M_f linearly decreases with the field at a rate dA_f/dH1.31 K T^{-1} and 1.82 K T^{-1} for the $Ni_{43}Mn_{45.3}B_{0.7}In_{11}$ and $Ni_{43}Mn_{45.0}B_{1.0}In_{11}$ alloys, respectively. The austenite phase is ferromagnetic while the martensite phase is antiferromagnetic at low fields, due to the interaction between Mn atoms in Mn and In sites. The application of a magnetic field shifted the martensitic transformation temperatures to lower temperatures and the magnetic field-induced phase transformation from martensite to austenite was confirmed. The large ΔM, sharp $\Delta M/\Delta T$, and almost full reversibility make the $Ni_{43}Mn_{45.0}B_{1.0}In_{11}$ alloy a potential candidate for magnetic shape memory, energy conversion, and solid-state refrigeration.

Data availability statement

All data that support the findings of this study are included within the article (and any supplementary files).

ORCID iDs

Oğuz Yildirim https://orcid.org/0000-0003-0957-9795
Baris Emre https://orcid.org/0000-0003-3468-7026

References

[1] Müllner P, Chernenko V A and Kostorz G 2004 Large cyclic magnetic-field-induced deformation in orthorhombic (14M) Ni–Mn–Ga martensite *J. Appl. Phys.* **95** 1531–6
[2] Ullakko K, Huang J K, Kantner C, O'handley R C and Kokorin V V 1996 Large magnetic-field-induced strains in Ni_2MnGa single crystals *Appl. Phys. Lett.* **69** 1966–8
[3] Karaca H E, Karaman I, Basaran B, Ren Y, Chumlyakov Y I and Maier H J 2009 Magnetic field-induced phase transformation in NiMnCoIn magnetic shape-memory alloys—a new actuation mechanism with large work output *Adv. Funct. Mater.* **19** 983–98
[4] Karaman I, Basaran B, Karaca H E, Karsilayan A I and Chumlyakov Y I 2007 Energy harvesting using martensite variant reorientation mechanism in a NiMnGa magnetic shape memory alloy *Appl. Phys. Lett.* **90** 172505
[5] Krenke T, Duman E, Acet M, Wassermann E F, Moya X, Mañosa L and Planes A 2005 Inverse magnetocaloric effect in ferromagnetic Ni–Mn–Sn alloys *Nat. Mater.* **4** 450–4
[6] Kihara T, Xu X, Ito W, Kainuma R and Tokunaga M 2014 Direct measurements of inverse magnetocaloric effects in metamagnetic shape-memory alloy NiCoMnIn *Phys. Rev.* B **90** 214409
[7] Monroe J A, Karaman I, Basaran B, Ito W, Umetsu R Y, Kainuma R, Koyama K and Chumlyakov Y I 2012 Direct measurement of large reversible magnetic-field-induced strain in Ni–Co–Mn–In metamagnetic shape memory alloys *Acta Mater.* **60** 6883–91
[8] Karaca H E, Karaman I, Brewer A, Basaran B, Chumlyakov Y I and Maier H J 2008 Shape memory and pseudoelasticity response of NiMnCoIn magnetic shape memory alloy single crystals *Scr. Mater.* **58** 815–8
[9] Wang B M, Liu Y, Ren P, Xia B, Ruan K B, Yi J B, Ding J, Li X G and Wang L 2011 Large exchange bias after zero-field cooling from an unmagnetized state *Phys. Rev. Lett.* **106** 077203
[10] Wang B M, Liu Y, Wang L, Huang S L, Zhao Y, Yang Y and Zhang H 2008 Exchange bias and its training effect in the martensitic state of bulk polycrystalline $Ni_{49.5}Mn_{34.5}In_{16}$ *J. Phys. D: Appl. Phys.* **104** 043916
[11] Wang B M, Ren P, Liu Y and Wang L 2010 Enhanced magnetoresistance through magnetic-field-induced phase transition in Ni_2MnGa co-doped with Co and Mn *J. Magn. Magn. Mater.* **322** 715–7
[12] Lin Y, Hao J, Qiao K, Gao Y, Hu F, Wang J, Zhao T and Shen B 2023 Phase transition regulation and caloric effect *Front. Energy* **17** 463–77
[13] Mañosa L, Planes A and Acet M 4925 Advanced materials for solid state refrigeration *J. Mater. Chem.* A **1** 4936
[14] Qian M, Zhang X, Wei L, Martin P, Sun J, Geng L, Scott T B and Peng H-X 2018 Tunable Magnetocaloric Effect in Ni-Mn-Ga Microwires *Sci. Rep.* **8** 16574
[15] Stern-Taulats E *et al* 2015 Tailoring barocaloric and magnetocaloric properties in low-hysteresis magnetic shape memory alloys *Acta Mater.* **96** 324–32
[16] Dubenko I, Samanta T, Kumar Pathak A, Kazakov A, Prudnikov V, Stadler S, Granovsky A, Zhukov A and Ali N 2012 Magnetocaloric effect and multifunctional properties of Ni–Mn-based Heusler alloys *J. Magn. Magn. Mater.* **324** 3530–4

[17] Yang J, Li Z, Zhang X, Yang B, Yan H, Cong D, Zhao X and Zuo L 2023 Manipulation of thermal hysteresis and magnetocaloric effect in the Ni-Co-Mn-In alloys through lattice contraction: effect of Ge substitution for In *Acta Mater.* **246** 118694

[18] Konieczny P, Sas W, Czernia D, Pacanowska A, Fitta M and Pełka R 2022 Magnetic cooling: a molecular perspective *Dalton Trans.* **51** 12762–80

[19] Tishin A M, Spichkin Y I, Zverev V I and Egolf P W 2016 A review and new perspectives for the magnetocaloric effect: new materials and local heating and cooling inside the human body *Int. J. Refrig.* **68** 177–86

[20] Tishin A M and Spichkin Y I 2016 *The Magnetocaloric Effect and Its Applications* (CRC Press)

[21] Planes A, Mañosa L and Acet M 2009 Magnetocaloric effect and its relation to shape-memory properties in ferromagnetic Heusler alloys *J. Phys. Condens. Matter* **21** 233201

[22] Pandey S, Quetz A, Aryal A, Dubenko I, Mazumdar D, Stadler S and Ali N 2017 Magnetocaloric, thermal, and magnetotransport properties of $Ni_{50}Mn_{35}In_{13.9}B_{1.1}$ Heusler alloy *J. Magn. Magn. Mater.* **444** 98–101

[23] Silva L E L, Patiño J C and Gomes A M 2021 On the structural and thermo-magnetic study of the magnetocaloric Heusler alloy $Ni_2Mn_{1-x}Cu_xGa_{0.8}Al_{0.2}$ *J. Phys. Condens. Matter* **33** 235701

[24] Beckmann B, Koch D, Pfeuffer L, Gottschall T, Taubel A, Adabifiroozjaei E, Miroshkina O N, Riegg S, Niehoff T and Kani N A 2023 Dissipation losses limiting first-order phase transition materials in cryogenic caloric cooling: a case study on all-d-metal Ni (-Co)-Mn-Ti Heusler alloys *Acta Mater.* **246** 118695

[25] Yuce S, Kavak E, Yildirim O, Bruno N M and Emre B 2023 Investigation of the inverse magnetocaloric effect with the fraction method *J. Phys.: Condens. Matter* **35** 345801

[26] Krenke T, Acet M, Wassermann E F, Moya X, Mañosa L and Planes A 2006 Ferromagnetism in the austenitic and martensitic states of Ni–Mn–In alloys *Phys. Rev.* B **73** 174413

[27] Umetsu R Y, Kusakari Y, Kanomata T, Suga K, Sawai Y, Kindo K, Oikawa K, Kainuma R and Ishida K 2009 Metamagnetic behaviour under high magnetic fields in $Ni_{50}Mn_{50-x}In_x$ (x = 14.0 and 15.6) shape memory alloys *J. Phys. Appl. Phys.* **42** 075003

[28] Sharma V K, Chattopadhyay M K and Roy S B 2007 Large inverse magnetocaloric effect in $Ni_{50}Mn_{34}In_{16}$ *J. Phys. Appl. Phys.* **40** 1869

[29] Oikawa K, Ito W, Imano Y, Sutou Y, Kainuma R, Ishida K, Okamoto S, Kitakami O and Kanomata T 2006 Effect of magnetic field on martensitic transition of $Ni_{46}Mn_{41}In_{13}$ Heusler alloy *Appl. Phys. Lett.* **88** 122507

[30] Law J Y, Díaz-García Á, Moreno-Ramírez L M, Franco V, Conde A and Giri A K 2019 How concurrent thermomagnetic transitions can affect magnetocaloric effect: the $Ni_{49+x}Mn_{36-x}In_{15}$ Heusler alloy case *Acta Mater.* **166** 459–65

[31] Pathak A K, Khan M, Dubenko I, Stadler S and Ali N 2007 Large magnetic entropy change in $Ni_{50}Mn_{50-x}$Inx Heusler alloys *Appl. Phys. Lett.* **90** 262504

[32] Wang L, Li Z, Yang J, Yang B, Zhao X and Zuo L 2020 Large refrigeration capacity in a $Ni_{48}Co_1Mn_{37}In_{14}$ polycrystalline alloy with low thermal hysteresis *Intermetallics* **125** 106888

[33] Kumar N P, Singh M, Mahey V, Nautiyal S, Kumar D M R, Rao N V R and Raja M M 2020 Effect of Si substitution on the structural, magnetic and magnetocaloric properties of Ni–Mn–In Heusler alloys *Appl. Phys.* A **126** 472

[34] Cicek M M, Saritas S, Yildirim O and Emre B 2020 Effect of the low constituent boron on martensitic transformation, magnetic, and magnetocaloric properties of $Ni_{50}Mn_{35}In_{15}$ Heusler alloys *J. Alloys Compd.* **845** 155493

[35] Sokolovskiy V V, Buchelnikov V D, Taskaev S V, Khovaylo V V, Ogura M and Entel P 2013 Quaternary Ni–Mn–In–Y Heusler alloys: a way to achieve materials with better magnetocaloric properties? *J. Phys. Appl. Phys.* **46** 305003

[36] Kaya M, Cicek M M, Dincer I and Elerman Y 2017 Magnetic and magnetocaloric properties of $Ni_{43}Mn_{46-x}Al_xIn_{11}$ (x = 0, 0.5 and 1.0) *J. Magn. Magn. Mater.* **442** 429–34

[37] Aydogdu Y, Turabi A S, Aydogdu A, Kok M, Yakinci Z D and Karaca H E 2016 The effects of boron addition on the magnetic and mechanical properties of NiMnSn shape memory alloys *J. Therm. Anal. Calorim.* **126** 399–406

[38] Luo H, Meng F, Jiang Q, Liu H, Liu E, Wu G and Wang Y 2010 Effect of boron on the martensitic transformation and magnetic properties of $Ni_{50}Mn_{36.5}Sb_{13.5-x}Bx$ alloys *Scr. Mater.* **63** 569–72

[39] Xuan H C, Wang D H, Zhang C L, Z D H, Gu B X and Du Y W 2008 Boron's effect on martensitic transformation and magnetocaloric effect in $Ni_{43}Mn_{46}Sn_{11}Bx$ alloys *Appl. Phys. Lett.* **92** 102503

[40] Mandru A-O, Yıldırım O, Marioni M A, Rohrmann H, Heigl M, Ciubotariu O-T, Penedo M, Zhao X, Albrecht M and Hug H J 2020 Pervasive artifacts revealed from magnetometry measurements of rare earth-transition metal thin films *J. Vac. Sci. Technol.* A **38** 023409

[41] Kılıç G, Abboosh O, Kırat G, Aksan M A, Aydoğdu A and Aydoğdu Y 2023 Investigation on the transport and magnetism properties of the boron-substituted NiMnSb *J. Therm. Anal. Calorim.* **148** 1–8

[42] Chernenko V A, Pons J, Seguı C and Cesari E 2002 Premartensitic phenomena and other phase transformations in Ni–Mn–Ga alloys studied by dynamical mechanical analysis and electron diffraction *Acta Mater.* **50** 53–60

[43] Díaz-García Á, Moreno-Ramírez L M, Law J Y, Albertini F, Fabbrici S and Franco V 2021 Characterization of thermal hysteresis in magnetocaloric NiMnIn Heusler alloys by temperature first order reversal curves (TFORC) *J. Alloys Compd.* **867** 159184

[44] Seiner H, Kopeček J, Sedlák P, Bodnárová L, Landa M, Sedmák P and Heczko O 2013 Microstructure, martensitic transformation and anomalies in c′-softening in Co–Ni–Al ferromagnetic shape memory alloys *Acta Mater.* **61** 5869–76

[45] Zuo S, Liang F, Zhang Y, Peng L, Xiong J, Liu Y, Li R, Zhao T, Sun J and Hu F 2018 Zero-field skyrmions generated via premartensitic transition in N i 50 M n 35.2 I n 14.8 alloy *Phys. Rev. Mater.* **2** 104408

[46] Gao B, Shen J, Hu F X, Wang J, Sun J R and Shen B G 2009 Magnetic properties and magnetic entropy change in Heusler alloys $Ni_{50}Mn_{35-x}Cu_xSn_{15}$ *Appl. Phys.* A **97** 443–7

[47] Khan M, Dubenko I, Stadler S, Jung J, Stoyko S S, Mar A, Quetz A, Samanta T, Ali N and Chow K H 2013 Enhancement of ferromagnetism by Cr doping in Ni-Mn-Cr-Sb Heusler alloys *Appl. Phys. Lett.* **102** 112402

[48] Xuan H C, Zhang Y Q, Li H, Han P D, Wang D H and Du Y W 2015 Effect of Ni/Sn ratio on martensitic transformation and magnetic properties in high-Mn content $Mn_2Ni_{1.64-x}Sn_{0.36+x}$ ferromagnetic shape memory alloys *Phys. Status Solidi* a **212** 680–5

[49] Wang D-H, Han Z-D, Xuan H-C, Ma S-C, Chen S-Y, Zhang C-L and Du Y-W 2013 Martensitic transformation and related magnetic effects in Ni—Mn-based ferromagnetic shape memory alloys *Chin. Phys.* B **22** 077506

[50] Bennett L H, Provenzano V, Shull R D, Levin I, Della Torre E and Jin Y 2012 Ferri- to ferro-magnetic transition in the

martensitic phase of a Heusler alloy *J. Alloys Compd.* **525** 34–38
[51] Yıldırım O, Yuce S, Bruno N M, Doğan E K, Yurtseven H, Duman E and Emre B 2022 Investigation of the complex magnetic behavior of $Ni_{46.86}Co_{2.91}Mn_{38.17}Sn_{12.06}$ (at%) magnetic shape memory alloy at low temperatures *Phys. Scr.* **97** 085806
[52] Emre B, Yıldırım O and Duman E 2019 Investigation of Ti substituting for Ni on magnetic, magnetocaloric and phase transition characteristics of $Ni_{50}Mn_{36}In_{14}$ *Mater. Res. Express* **6** 076102
[53] Krenke T, Acet M, Wassermann E F, Moya X, Mañosa L and Planes A 2005 Martensitic transitions and the nature of ferromagnetism in the austenitic and martensitic states of Ni− Mn− Sn alloys *Phys. Rev.* B **72** 014412
[54] Swathi S, Arun K, UD R, SR A, Dzubinska A, Reiffers M and Nagalakshmi R 2023 $Ni_{48}Ag_2Mn_{37}In_{13}$ multifunctional alloy: a room temperature inverse magnetocaloric and magnetoresistive material *J. Alloys Compd.* **938** 168590
[55] Cavazzini G, Cugini F, Gruner M E, Bennati C, Righi L, Fabbrici S, Albertini F and Solzi M 2019 Tuning the magnetic and magnetocaloric properties of austenitic Ni-Mn-(In,Sn) Heuslers *Scr. Mater.* **170** 48–51
[56] Lázpita P, L'vov V A, Fernández J R, Barandiarán J M and Chernenko V A 2020 Combined effect of magnetic field and hydrostatic pressure on the phase transitions exhibited by Ni-Mn-In metamagnetic shape memory alloy *Acta Mater.* **193** 1–9
[57] Krenke T, Aksoy S, Duman E, Acet M, Moya X, Mañosa L and Planes A 2010 Hysteresis effects in the magnetic-field-induced reverse martensitic transition in magnetic shape-memory alloys *J. Phys. D: Appl. Phys.* **108** 043914
[58] Anon Caron L, Ou Z Q, Nguyen T T, Thanh D C, Tegus O and Brück E 2009 On the determination of the magnetic entropy change in materials with first-order transitions *J. Magn. Magn. Mater.* **321** 3559–66
[59] Kavita S, Ramakrishna V V, Yadav P, Kethavath S, Lalla N P, Thomas T, Bhatt P and Gopalan R 2019 Enhancement of martensite transition temperature and inverse magnetocaloric effect in $Ni_{43}Mn_{47}Sn_{11}$ alloy with B doping *J. Alloys Compd.* **795** 519–27
[60] Huang L, Cong D Y, Ma L, Nie Z H, Wang Z L, Suo H L, Ren Y and Wang Y D 2016 Large reversible magnetocaloric effect in a Ni-Co-Mn-In magnetic shape memory alloy *Appl. Phys. Lett.* **108** 032405
[61] Pandey S, Quetz A, Ibarra-Gaytan P J, Sanchez-Valdes C F, Aryal A, Dubenko I, Mazumdar D, Sanchez Llamazares J L, Stadler S and Ali N 2018 Effects of annealing on the magnetic properties and magnetocaloric effects of B doped Ni-Mn-In melt-spun ribbons *J. Alloys Compd.* **731** 678–84
[62] Pandey S, Quetz A, Ibarra-Gaytan P J, Sánchez-Valdés C F, Aryal A, Dubenko I, Sanchez Llamazares J L, Stadler S and Ali N 2018 Magnetostructural transitions and magnetocaloric effects in $Ni_{50}Mn_{35}In_{14.25}B_{0.75}$ ribbons *AIP Adv.* **8** 056434